Journal of Materials Chemistry A

ROYAL SOCIETY OF CHEMISTRY

PAPER

View Article Online
View Journal | View Issue

Cite this: *J. Mater. Chem. A*, 2020, 8, 3918

Functional transformation of four-bladed rylene propellers utilizing non-metal and d^8 metal core shifting strategy: significant impact on photovoltaic performance and electrocatalytic hydrogen evolution activity†

Jianhua Han,[a] Wenwen Shi,[b] Xunchang Wang,[a] Jingwen Cai,[c] Xinyu Hao,[c] Jingying Shi,[b] Xichang Bao *[a] and Renqiang Yang *[a]

Two kinds of four-bladed perylene diimide (PDI) propellers with d^8 metal and non-metal cores are efficiently synthesized. The Ni-PDI, Pd-PDI, and Pt-PDI propellers, equipped with d^8 metal cores, have two absorption bands at 350–650 nm and 780–1200 nm with deep LUMO levels of —4.40 eV to —4.51 eV. The TTF-PDI, QU-PDI, and PH-PDI propellers with non-metal cores have only one absorption band at 350–650 nm with upshifted LUMO levels. Interestingly, the organic photovoltaic (OPV) results show that reducing the intramolecular charge traps between the blade and core subunits of the PDI propellers can effectively improve the power conversion efficiency (PCE). The device based on the QU-PDI acceptor exhibits a PCE that is up to more than 300 times higher (9.33%) than that of the d^8 metal core PDI propellers (Pd-PDI, PCE ¼ 0.03%), which is one of the best photovoltaic performances with an excellent fill factor (FF ¼ 71.8%) exhibited by PDI-derivative acceptors. Conversely, the electro-catalytic H_2 evolution activity of Pt-PDI (current destiny ¼ 10.00 mA cm^{-2} at —0.377 V), which exhibited a record performance for PDI-based catalysts to date, is up to 1000 times greater than that of the non-metal core PDI propellers (QU-PDI, 0.01 mA cm^{-2} at —0.377 V). Our results indicate that both highly efficient OPV and electrochemical H_2 evolution catalysts can be achieved *via* the rational functionalization of PDI propellers with non-metal and d^8 metal cores.

Received 13th January 2020
Accepted 30th January 2020

DOI: 10.1039/d0ta00506a

rsc.li/materials-a

1. Introduction

Rylene dyes, which have extended electron affinity conjugated skeletons, have attracted extensive attention due to their unique molecular chemical structures, remarkable electro-optical physical properties, impressive self-assembly behaviors, and fascinating applications in various 珋elds and have great potential for use as high-performance n-type organic semiconductors, for example, the perylene diimide (PDI) moieties used in non-fullerene organic photovoltaic (OPV) 珋elds.[1–9] To prohibit large crystalline aggregate domains in the active layer of OPV devices, various nonplanar blade-core-like PDI propeller architectures were designed *via* functionalization in the bay, alpha or imide group regions of PDIs.[10–13] Such nonplanar propellers are typically obtained using PDI moieties as blades and embedding two-, three-, four-, 珋ve- or six-armed cores with pi-bridge, ring-fusion or cycloaromatization strategies.[10,14–19] The relationship between the structural features of the blade-core effect and intramolecular interactions has been investigated and is important for expanding the potential applications of blade-core-like PDI propellers.

Neutral d^8 metal bis-dithiolene complexes possessing unique conductivity, magnetism and photophysical properties have attracted growing attention for applications in opto-electronic 珋elds[20] for use as thermoelectric materials, reversible binding/release of ole珋ns, superconducting materials, photochemical materials, electrochemical materials and photoelectrochemical water reduction catalysts.[21–25] The electronic structures around the Frontier orbitals and properties of these neutral d^8 metal bis-dithiolene complexes are mainly in珠uenced by the effective nuclear charge and relativistic potential of the metal core, such as the metal d-orbital energy levels, which are relative to those of ligand-based orbitals. Taking a close look at neutral d^8 metal bis-dithiolene structures, the topology of

[a]CAS Key Laboratory of Bio-Based Materials, Qingdao Institute of Bioenergy and Bioprocess Technology, Chinese Academy of Sciences, Qingdao 266101, China. E-mail: baoxc@qibebt.ac.cn; yangrq@qibebt.ac.cn

[b]State Key Laboratory of Catalysis, Dalian Institute of Chemical Physics, Chinese Academy of Sciences, Dalian National Laboratory for Clean Energy, Dalian 116023, China

[c]State Key Laboratory of Fine Chemicals, Dalian University of Technology, Dalian 116024, China

† Electronic supplementary information (ESI) available: Comprehensive experimental details and supplementary results. See DOI: 10.1039/d0ta00506a

such complexes featuring four functionalized reactive sites adopts an ingenious four-blade-core-like molecular con丽guration, which provides an opportunity to introduce promising electrophilic PDI moieties as blade subunits into the neutral d^8 metal bis-dithiolene core.

Inspired by the chemical and physical features of PDIs and neutral d^8 metal bis-dithiolene complexes, herein, we designed and synthesized six different four-bladed PDI propellers with d^8 metal and non-metal cores, as shown in Fig. 1. The exceptional chemical and physical characteristics of the neutral d^8 metal bis-dithiolene complexes strongly depended on the central metal types. Therefore, Ni, Pd and Pt metal-based bis-dithiolene cores were introduced into rylene propellers with four PDI blades, and these resulting complexes were named Ni-PDI, Pd-PDI and Pt-PDI, respectively. To provide deep insight into the core effect of the structure–property relationship, three non-metal cores were also embedded into the PDI propellers. TTF-PDI with a tetrathiafulvalene (TTF) core has a molecular structure similar to that of the d^8 metal bis-dithiolene core. The quinone is justi丽ed by a topological analogy of the p-electron system of d^8 metal bis-dithiolene complexes.[26] Thus, a benzoquinone core was introduced into the PDI propeller, which was named QU-PDI. PH-PDI with a benzene core was synthesized for comparison. It is found that fewer intramolecular charge traps between the blade and core subunits of the PDI propeller acceptors will signi丽cantly improve the OPV performances. The device based on the QU-PDI acceptor exhibits a power conversion efficiency (QU-PDI, PCE¼ 9.33%) that is up to more than 300 times higher than that of the d^8 metal core and TTF core-based PDI propellers (Pd-PDI, PCE ¼ 0.03%) by reducing the intramolecular charge traps. This is one of the best photovoltaic performances among the devices based on PDI-based acceptors (see Fig. S50 and Table S7†). In addition, 0D, 1D and 2D complex catalysts containing metal bis-dithiolene moieties exhibit potential applications for photocatalytic and electrochemical hydrogen evolution reactions (HERs).[21] Metal complex

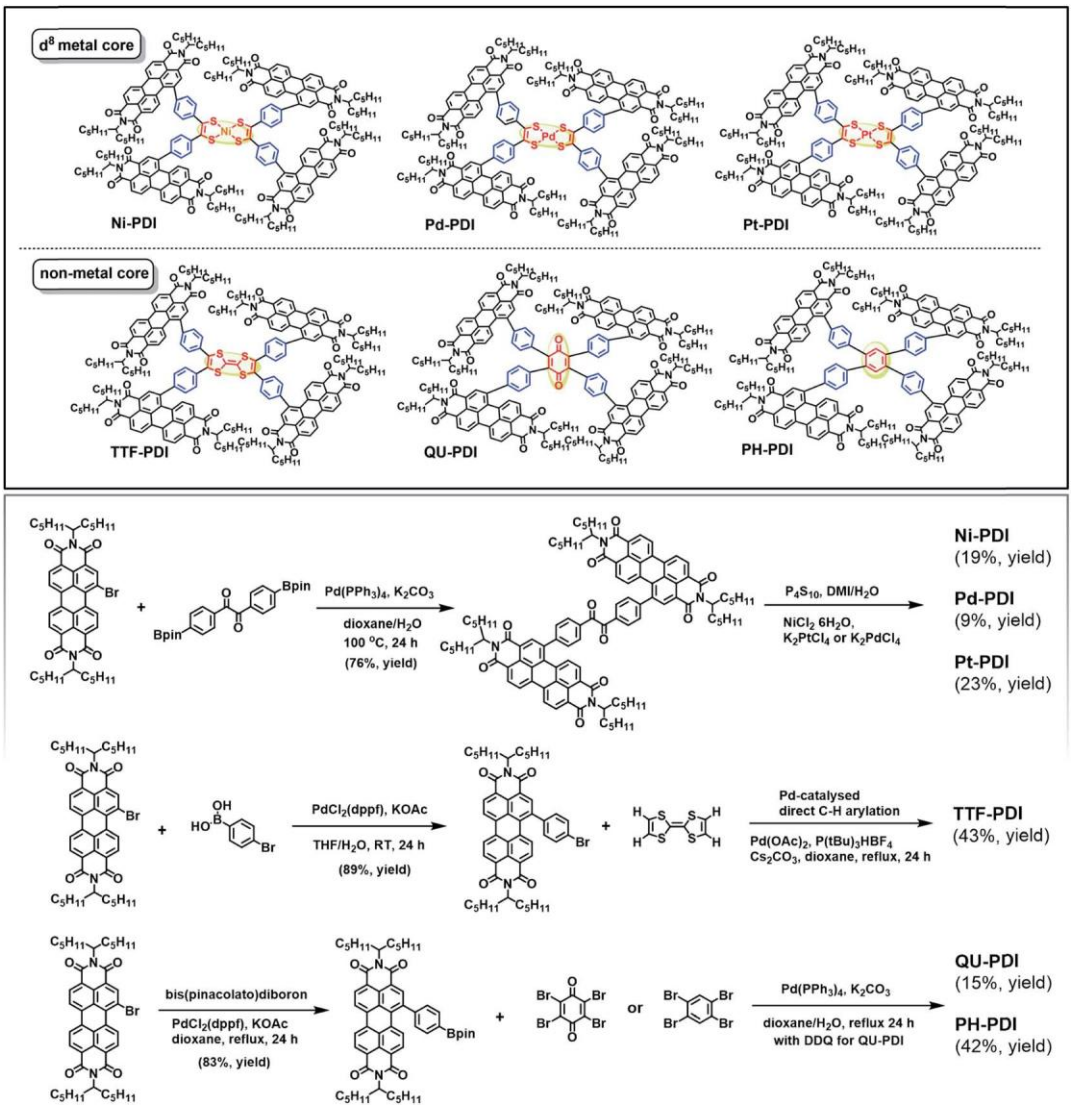

Fig. 1 Structures, synthetic route and isolated yield for six four-bladed PDI propellers with d^8 metal and non-metal cores.

catalysts have also attracted great interest because of their intriguing structural diversities and interesting properties, such as their photoluminescence, magnetic and electrochemical catalytic properties.[27–30] Understanding the role of metal ions and coordination environments is of great importance to design high performance catalysts. Herein, Ni-PDI, Pd-PDI and Pt-PDI were used as electrocatalytic water reduction catalysts to understand the effect of metal ions on hydrogen production, and we also compared Pt-PDI with another Pt complex without a PDI ligand (Pt-PH) to study the effect of the ligand on the HER activity. As a result, the HER efficiency increases in the order of Pd $4d^8$ < Ni $3d^8$ « Pt $5d^8$ for the three d^8 metal-based PDI propellers. Additionally, compared with Pt-PH, the PDI moieties in Pt-PDI and the propeller architectures minimize catalyst aggregation and increase the electrochemical surface area with an enhanced HER efficiency. In contrast to the OPV performances, the HER activity of the Pt-PDI catalyst (current destiny ¼ 10.00 mA cm^{-2} at —0.377 V) is up to approximately 1000 times greater than that of the non-metal core PDI propellers catalysts (QU-PDI, only 0.01 mA cm^{-2} at –0.377 V). To summarize, these advances in nonplanar four-bladed PDI propellers with d^8 metal and non-metal cores will aid the synthesis and functionalization of blade-core-like rylene dyes and expand their applications in OPV devices and electrochemical hydrogen production.

2. Results and discussion

2.1 Synthesis and characterization

The procedure used to synthesize the six four-bladed rylene propellers is shown in Fig. 1 (for details, see Fig. S1–S5†). Three propellers with d^8 metal cores were synthesized through sulfuration of the original benzil proligands appended with PDI moieties in 1,3-dimethyl-2-imidazolidinone (DMI), which was followed by the hydrolysis of the intermediate phosphorous thioesters with nickel salt ($NiCl_2$\$$6H_2O$), palladium salt ($K_2PdCl_4$) or platinum salt ($K_2PtCl_4$) to directly afford the neutral nickel complex Ni-PDI, palladium complex Pd-PDI and platinum complex Pt-PDI.[31] Due to the steric hindrance effect and low reactivity of such large sized PDI-type ligands, the yields of Ni-PDI and Pt-PDI are as low as 19% and 23%, which are lower than most of the d^8 metal complex yields.[32] More detailed by-product analyses of the complex reactions are shown in Fig. S32–S35.† We also noticed that the silica gel tended to degrade the Pd complex, and thus, the yield of Pd-PDI is quite low, 9%.

For the three non-metal core PDI propellers, TTF-PDI is synthesized by the palladium-catalysed direct C–H arylation of tetrathiafulvalene with PDI bromides in the presence of caesium carbonate and a palladium catalyst.[33] QU-PDI and PH-PDI are prepared by typical Suzuki–Miyaura coupling reactions with $Pd(PPh_3)_4$ as the catalyst and dioxane/H_2O as the solvent, according to the literature method.[4,34] The PDI moiety contains branched alkyl chains to ensure the good solubility of the four-bladed PDI propellers in chlorobenzene and chloroform. The chemical structures of the six PDI propellers are completely characterized by ^{1}H-NMR spectroscopy, ^{13}C-NMR spectroscopy (Fig. S6–S17†), HRMS spectrometry (Fig. S26–S31†) and an elemental analysis. The chemical shi泗s of the proton for Ni-PDI, Pd-PDI and Pt-PDI can be easily distinguished (Fig. S18†). Furthermore, the chemical shi泗s of the carbon of the C]C bond in the d^8 metal dithiolene core can also be distinguished at 180.92 ppm (Ni-PDI), 180.02 ppm (Pd-PDI) and 177.23 ppm (Pt-PDI), as shown in Fig. S19.† Thermogravimetric analysis (TGA) and differential scanning calorimetry (DSC) are performed to investigate the thermal properties of the PDI propellers. The PDI propellers except for Pt-PDI retained 95% of their weight up to 372–398 °C; Pt-PDI was thermally unstable at 259 °C in a nitrogen atmosphere (Fig. S36A†). All six PDI propellers are relatively amorphous and exhibit no signal corresponding to a melting transition (Fig. S36B†).[14]

2.2 Optical and electrochemical properties

The UV-vis-NIR absorption spectra of the six PDI propellers in a dilute chloroform solution and thin 珋lms are shown in Fig. 2, and the corresponding data are summarized in Table 1. In the chloroform solution, absorption by the three d^8 metal core PDI propellers is exhibited by two bands: 350–650 nm and 780–1200 nm. The visible range absorption centred around 530–552 nm is a classic characteristic of a PDI moiety.[10,35] The low energy absorption band is attributed to the neutral metal-bis(dithiolene) cores and corresponds to an electronic transition from the HOMO (L_p) of the b_{1u} symmetry to the LUMO ðL_p^*— ad_{xy}Þ with the metallic character of the b_{2g} symmetry.[20] The maximum absorption wavelengths of Ni-PDI, Pd-PDI and Pt-PDI in the near infrared (NIR) region are 884 nm, 914 nm and 822 nm, respectively. The corresponding absorption extinction coefficients of the d^8 metal-based PDI propellers are in the range of 1.10×10^4 M^{-1} cm^{-1} to 1.32×10^4 M^{-1} cm^{-1}. In the visible absorption area, the maximum absorption wavelengths

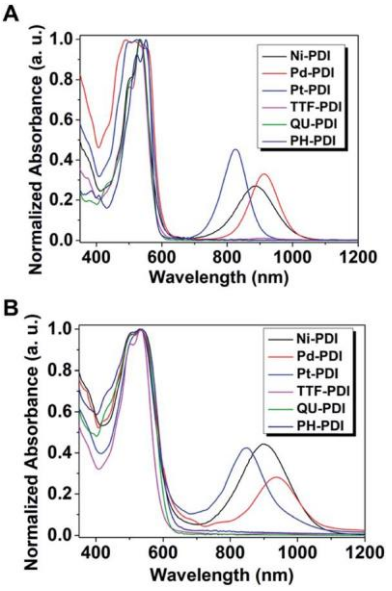

Fig. 2 UV-vis-NIR absorption spectra of the PDI propellers. (A) UV-vis-NIR absorption spectra of the PDI propellers in the chloroform solution. (B) UV-vis-NIR absorption spectra of the PDI propellers in thin films.

Table 1 Summary of the optical and electronic properties of the PDI propellers

	UV-vis range (350 nm to 780 nm)			NIR range (780 nm to 1200 nm)							
Propellers	λ_{max}^{film} (nm)	$\lambda_{max}^{sol\ a}$ (nm)	ε_{max} (M^{-1} cm^{-1})	λ_{max}^{film} (nm)	λ_{max}^{sol} (nm)	ε_{max} (M^{-1} cm^{-1})	$LUMO^{CVb}$ (eV)	$HOMO^{CVc}$ (eV)	E_g^{optd} (eV)	$LUMO^{DFTe}$ (eV)	$HOMO^{DFT}$ (eV)	E_g^{DFT} (eV)
Ni-PDI	530	531	4.92×10^4	898	884	1.32×10^4	−4.40	−5.58	1.18	−4.45	−6.11	1.66
Pd-PDI	534	532	3.84×10^4	937	914	1.27×10^4	−4.42	−5.57	1.16	−4.48	−6.11	1.63
Pt-PDI	533	532	4.95×10^4	849	822	1.10×10^4	−4.51	−5.77	1.26	−4.41	−6.24	1.83
TTF-PDI	533	534	3.29×10^4	926	912	330	−3.91	−6.01	2.10	−3.10	−5.66	2.56
QU-PDI	532	536	3.89×10^4	—	—	—	−4.03	−6.02	2.05	−3.23	−6.40	3.17
PH-PDI	532	552	3.44×10^4	—	—	—	−3.88	−5.93	1.99	−3.11	−6.29	3.19

[a] Measured in the $CHCl_3$ solution. [b] Calculated according to $E_{LUMO} = (E_{HOMO} - E_g^{opt})$ eV. [c] Estimated from the onset potential of the first oxidation wave (vs. F_c/F_c^+) and calculated according to $E_{HOMO} = -(4.8 + E_{onset})$ eV. [d] Obtained from the edge of the absorption spectra in the films according to $E_g^{opt} = (1240/\lambda_{onset})$. [e] Calculated by DFT.

of Ni-PDI, Pd-PDI and Pt-PDI are approximately 531 nm and 532 nm, with absorption extinction coefficients from 3.84×10^4 M^{-1} cm^{-1} to 4.95×10^4 M^{-1} cm^{-1}. In the thin films, the absorption spectra of the three d^8 metal core PDI propellers also exhibit two bands at 400–600 nm and 700–1200 nm, as shown in Fig. 2B, which is similar to the absorption distribution observed in the chloroform solutions.

Without d^8 metal cores, QU-PDI and PH-PDI exhibit only one broad absorption band in the range of 350–650 nm (no NIR absorption) in the chloroform solution. QU-PDI has an extinction coefficient of 3.89×10^4 M^{-1} cm^{-1} at 536 nm, which is higher than that of PH-PDI (3.44×10^4 M^{-1} cm^{-1} at 552 nm). TTF-PDI exhibits the weakest absorption among the six PDI propellers in the dilute chloroform solution, with an extinction coefficient of 3.29×10^4 M^{-1} cm^{-1} at 534 nm. Interestingly, an NIR absorption band at 912 nm with a low extinction coefficient (330 M^{-1} cm^{-1}) can be observed for TTF-PDI (see Fig. S40†). Different from the well-known d^8 metal bis-dithiolene NIR absorbing dyes,[20,36] the neat PDI moiety or tetrathiafulvalene core does not absorb between 900 and 1100 nm. When the TTF core and PDI blade are combined, NIR absorption at 912 nm (in the solution) and 926 nm (in the thin film) occurs for TTF-PDI. Generally, simply extending the conjugated length of the PDI propellers, as done in TTF-PDI, is not enough to prolong the absorption wavelength to the NIR range of approximately 926 nm. Herein, we deduce that the PDI blade can associate with the core subunit (TTF moiety), resulting in a charge transfer effect. In the TTF-PDI molecule, the PDI blades adjacent to the TTF core induce charge transfer when the offset between the HOMO of the electron-donating TTF unit and the LUMO of the electron-deficiency PDI unit is sufficient to provide a thermodynamic driving force for electron transfer.[37,38] These observations of NIR absorption and charge transfer behaviours in the solution and film states are similar to the behaviours of P3HT/F_4TCNQ and PBTTT-C_{14}/F_4TCNQ.[39,40]

The electrochemical properties of the six PDI propellers were measured by cyclic voltammetry (Fig. S37†) and summarized in Table 1. For the three d^8 metal core PDI propellers, the LUMO values are estimated to be −4.40 eV (Ni-PDI), −4.42 eV (Pd-PDI) and −4.51 eV (Pt-PDI), which are much lower than the values of the three non-metal core PDI propellers: −3.91 eV (TTF-PDI), −4.03 eV (QU-PDI) and −3.88 eV (PH-PDI). Owing to the metal-bis(dithione) core effect, the E_g^{opt} values are 1.16 eV (Pd-PDI) < 1.18 eV (Ni-PDI) < 1.26 eV (Pt-PDI), which are much lower than those of non-metal core PDI propellers. Without the d^8 metal cores, the band gap of TTF-PDI, QU-PDI and PH-PDI is 2.10 eV, 2.05 eV and 1.99 eV, respectively. The HOMO and LUMO levels are also determined by density functional theory (DFT) calculations and ultraviolet photoelectron spectroscopy (UPS). As shown in Table 1 and Fig. S39,† the tendency of the values obtained by DFT and UPS is consistent with the values obtained by cyclic voltammetry measurements.

2.3 Photovoltaic performances

Solution-processed bulk-heterojunction (BHJ) organic solar cells based on the six PDI propellers were fabricated with

a conventional device configuration of ITO/PEDOT:PSS/PBDB-TFCl:PDI propellers/PDINO/Al, where ITO is indium tin oxide, PEDOT:PSS is poly(3,4-ethylenedioxythiophene):poly(styrene sulfonate) and PDINO is *N*,*N*-dioxide of bis(*N*,*N*′-dimethylaminopropyl) perylene diimide.[41] Terpolymer PBDB-TFCl is used as the donor material (Fig. 3A and B) due to its matched energy levels.[42] The current density–voltage (*J*–*V*) characteristics of the optimal devices are shown in Fig. 3C and D, and the related device parameters are summarized in Table 2. The optimization details are shown in Tables S1–S6.†

For the photovoltaic devices based on the three d^8 metal core PDI propellers, extremely low PCEs of 0.03% to 0.07% were obtained, with poor open circuit voltages (V_{OC}) of 0.43 V to 0.51 V, low short-circuit currents (J_{SC}) of 0.21 mA cm^{-2} to 0.53 mA cm^{-2}, and low fill factors (FF) of 32.3% to 34.9%. Such a poor V_{OC} is due to the lower-lying LUMO level of Ni-PDI, Pd-PDI and Pt-PDI. For the non-metal core propellers, TTF-PDI possesses an appropriately upshifted LUMO level (−3.91 eV) and a molecular configuration similar to that of Ni-PDI, Pd-PDI and Pt-PDI. However, a low PCE of 0.18% was obtained with an

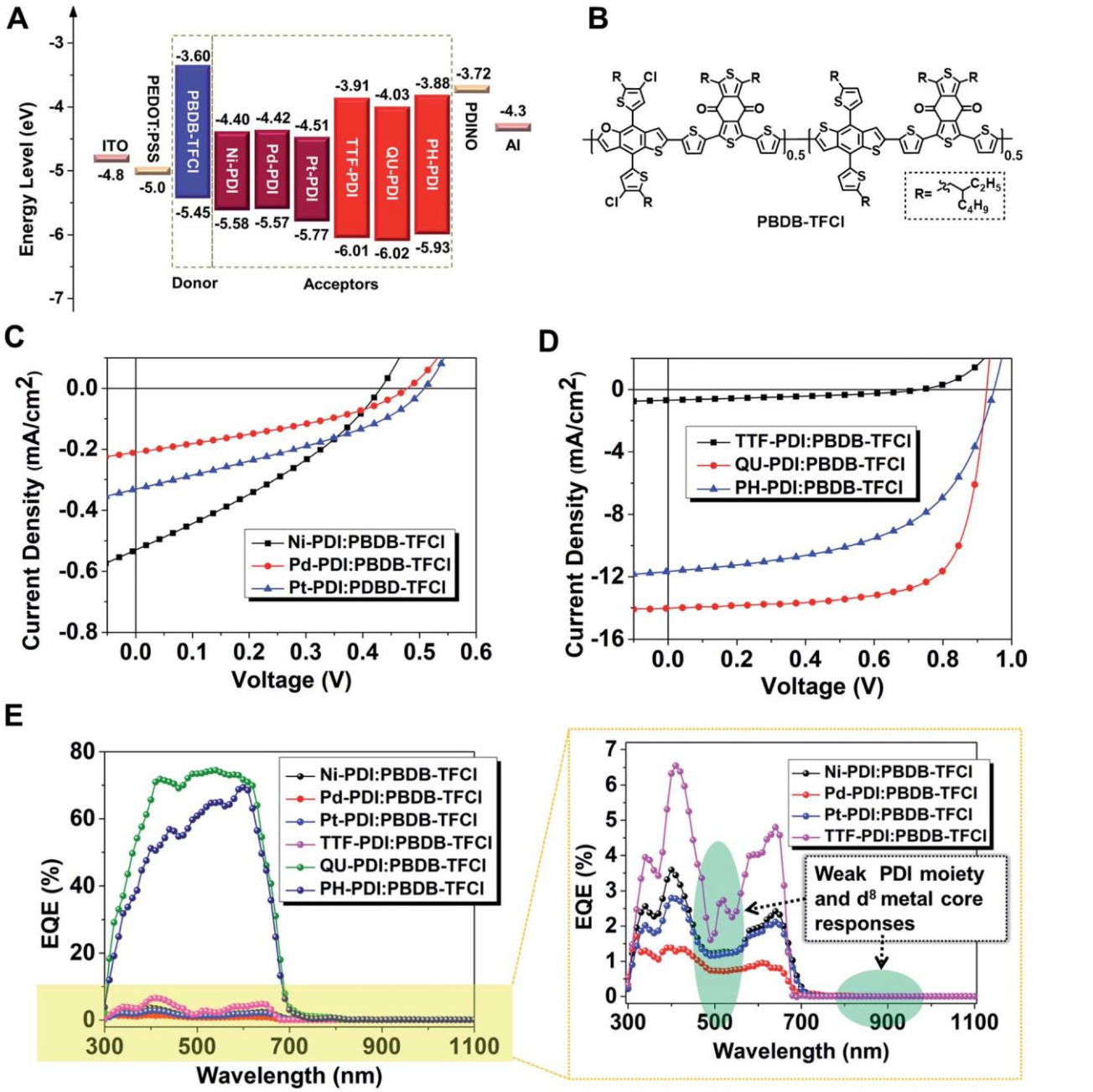

Fig. 3 OPV properties of the six PDI propellers. (A) Energy level diagrams of all the materials used in the solar cell device. (B) Chemical structure of PBDB-TFCl. (C) *J*–*V* curves of the photovoltaic devices based on the PBDB-TFCl:d^8 metal core PDI propellers. (D) *J*–*V* curves of the photovoltaic devices based on the PBDB-TFCl:non-metal core PDI propellers under AM 1.5G irradiation (100 mW cm^{-2}). (E) External quantum efficiency spectra of the PDI-based solar cells.

Table 2 Photovoltaic parameters of the optimized PBDB-TFCl:PDI propeller solar cells under AM 1.5G Illumination at 100 mW cm^{-2}

Acceptor	V_{OC} (V)	J_{SC} (mA cm^{-2})	FF (%)	PCE[a] (%)
Ni-PDI	0.43 (0.43 ± 0.01)	0.53 (0.49 ± 0.04)	32.3 (32.5 ± 0.8)	0.07 (0.07 ± 0.00)
Pd-PDI	0.47 (0.46 ± 0.01)	0.21 (0.21 ± 0.00)	34.9 (35.2 ± 0.5)	0.03 (0.03 ± 0.00)
Pt-PDI	0.51 (0.50 ± 0.01)	0.33 (0.32 ± 0.01)	34.2 (34.1 ± 0.4)	0.06 (0.06 ± 0.00)
TTF-PDI	0.73 (0.73 ± 0.00)	0.69 (0.63 ± 0.04)	35.3 (35.2 ± 0.2)	0.18 (0.16 ± 0.01)
QU-PDI	0.93 (0.91 ± 0.02)	14.02 (14.17 ± 0.75)	71.8 (69.4 ± 2.8)	9.33 (8.91 ± 0.24)
PH-PDI	0.95 (0.97 ± 0.01)	11.66 (10.69 ± 0.58)	54.4 (52.4 ± 1.8)	6.01 (5.41 ± 0.36)

[a] The efficiency value was calculated from ten devices. The highest PCE values are shown in the parentheses. The optimization details are shown in Tables S1–S6.

increased V_{OC} of 0.73 V, and a similarly low J_{SC} of 0.69 mA cm^{-2} and low FF of 35.3% were obtained. More details will be discussed later. The photovoltaic devices based on QU-PDI and PH-PDI exhibit an impressive PCE of 9.33% and 6.01% with a V_{OC} of 0.93 V and 0.95 V, a J_{SC} of 14.02 mA cm^{-2} and 11.66 mA cm^{-2}, and an FF of 71.8% and 54.4%. The statistical PCE distribution histograms of 25 PBDB-TFCl:QU-PDI solar cells are shown in Fig. S48.† What is more, the PCE of the QU-PDI acceptor device is more than 300 times higher (9.33%) than that of the d^8 metal core PDI propeller acceptor (Pd-PDI, 0.03%). The external quantum efficiency (EQE) spectra are shown in Fig. 3E. The d^8 metal core-based PDI and TTF-PDI exhibit extremely low EQE values with a weak PDI moiety (*ca.* 530 nm) response and no d^8 metal core (*ca.* 900 nm) response. One can 珋nd that the V_{OC}, J_{SC} and FF values in the QU-PDI and PH-PDI-based solar cells are much higher than those in the solar cells based on the d^8 metal core PDI propellers and TTF-PDI. These results indicate that the cores play a critical role for the PDI propeller acceptors, which can greatly in珠uence their photovoltaic performances.

2.4 Theoretical analysis and 珋lm morphological characterizations

DFT was employed using the hybrid BLYP35 function to obtain the optimal 3D molecular geometries.[32,43] To facilitate the calculation, the branched alkyl chains were simpli珋ed to methyl groups. For the valence and core electrons of the S atoms and metal atoms, the double-x quality LANL2DZ basis set and the Los Alamos effective core potentials were used. For all the other atoms, the 6-31G* basis set was used. All four-blade PDI propellers exhibit 3D nonplanar con珋gurations to suppress intermolecular stacking and aggregation, as shown in Fig. 4. The dihedral angles between PDI and the benzene bridge, q_a, are in the range of 57.7° to 61.7°. The dihedral angle q_b between the benzene bridge and the core is in the range of 48.3° to 58.2°. This could effectively reduce the excessive aggregations and intermolecular interactions of the PDI propellers.[3,44,45]

Atomic force microscopy (AFM) and transmission electron microscopy (TEM) measurements were performed to investigate the morphological properties. As displayed in Fig. S49,† all the blended 珋lms have smooth surfaces with a root-mean-square (RMS) roughness of 0.667 nm to 0.841 nm. The TEM patterns demonstrate that nanoscale networks form in the active layer. Grazing incidence wide angel X-ray scatterings (GIWAXS) patterns were used to investigate the micro-structure of the pristine PDI 珋lms and polymer:PDI acceptor blended 珋lms. The corresponding patterns and intensity pro珋les are shown in Fig. 5. The pristine PDI 珋lms exhibit ring-like scattering peaks and randomly orient in the thin 珋lms with a p–p stacking distance of approximately 4.27 Å, indicating that their isotropic transport behaviours are quite similar to those of fullerene derivatives[46–49] and reported PDI analogues.[1,14,16,50–53] This is also consistent with the propeller-shaped molecular geometry with reduced aggregations, as calculation by DFT in Fig. 4. The neat

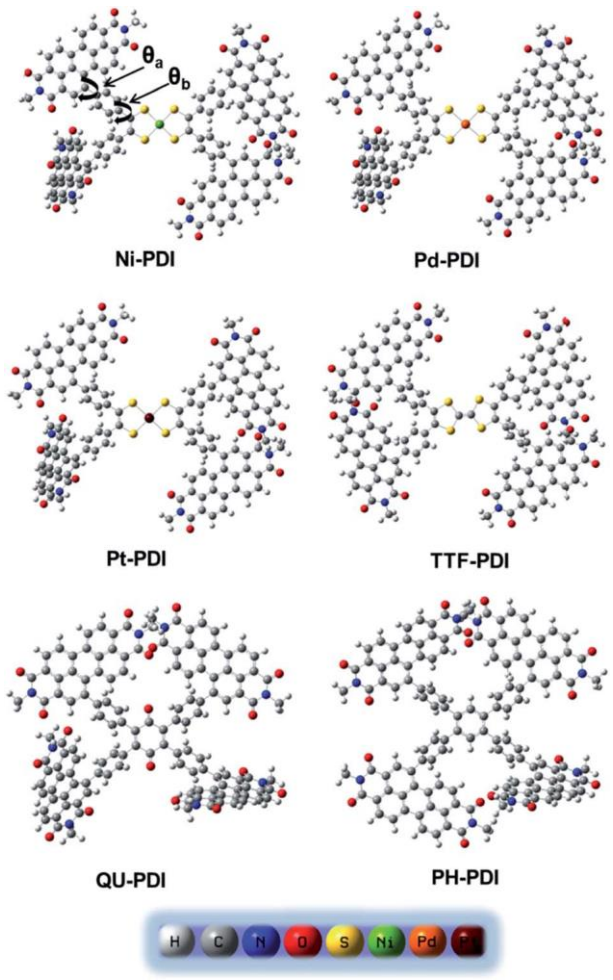

Fig. 4 Optimal molecular geometries of the six PDI propellers using DFT calculations.

PBDB-TFCl 薄lm exhibits strong peaks corresponding to lamellar (100) and (001) stacking, and a (010) p–p stacking diffraction peak in the out-of-plane direction is observed at 4.19 Å (in Fig. 5D). In the blended 薄lms, note that the stacking diffraction peak distances for these BHJ 薄lms are slightly different. The morphologies of the six blended 薄lms are mainly controlled by the polymer donor and PDI acceptor. The six PDI propellers possess similar molecular con薄gurations, resulting in the similar interactions between the donor and PDI propeller acceptors. The morphology features of these blended 薄lms are also similar to that of typical donor/PDI-acceptor systems and should not be detrimental to the charge dynamics and device performance due to such substantial differences.[15,16,18,44,54,55]

2.5 Dissociation and recombination

The electron and hole carrier mobilities of the six PDI propeller blended 薄lms were measured with the space charge limit current (SCLC) method to understand the relationship between the materials and photovoltaic performances (data in Table 3, curves in Fig. S45 and S46†). The electron mobilities are 4.16×10^{-6} cm^2 V^{-1} s^{-1}, 5.53×10^{-6} cm^2 V^{-1} s^{-1},

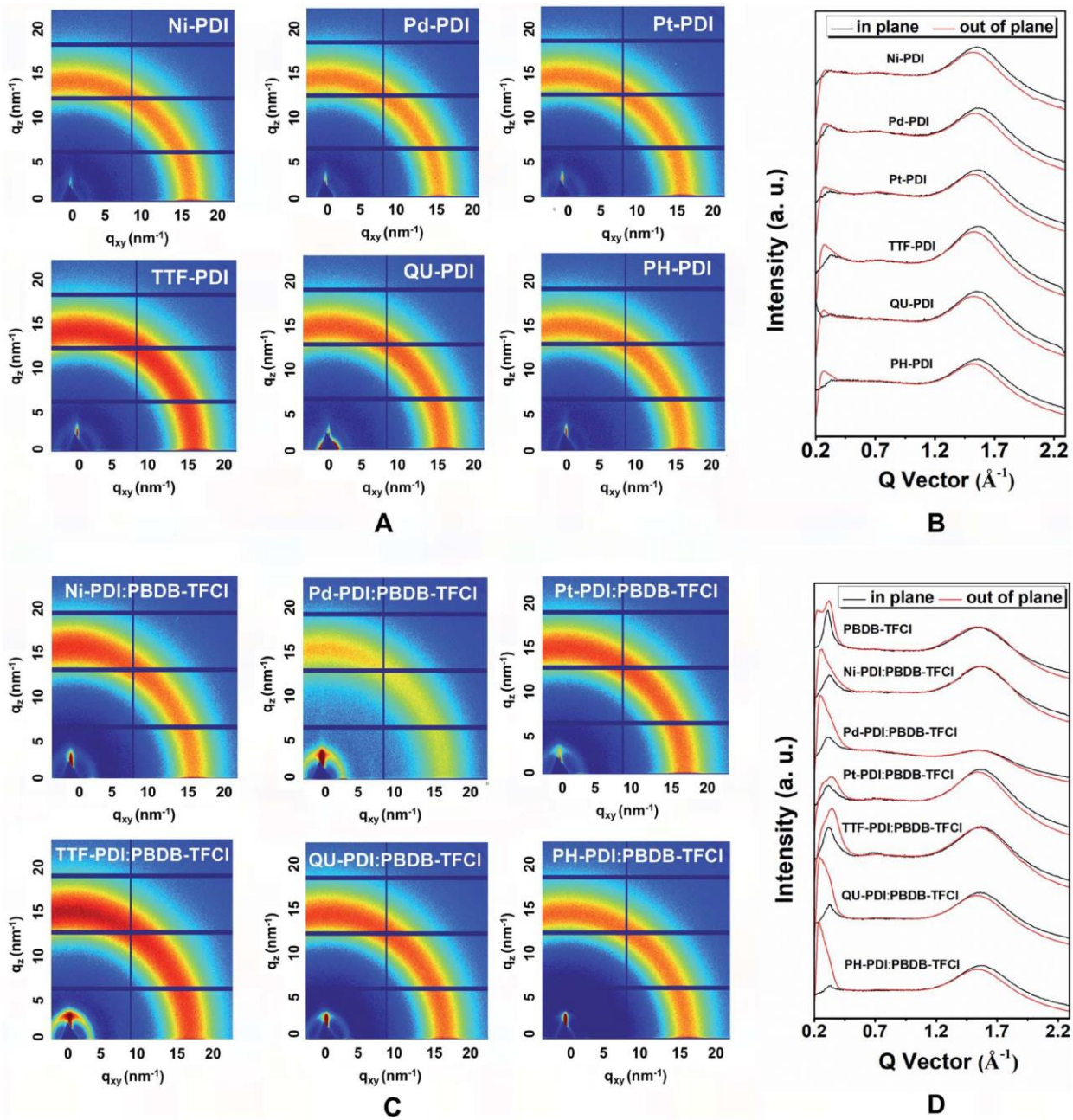

Fig. 5 Grazing incidence wide angel X-ray scattering patterns and line-cut profile results. (A) GIWAXS of the neat PDI propellers. (B) Line-cut profiles of the GIWAXS results obtained for the neat PDI propellers. (C) GIWAXS of the BHJ films. (D) Line-cut profiles of the GIWAXS results obtained for the BHJ films.

Table 3 Hole and electron mobilities of the optimized PBDB-TFCl:PDI propeller acceptor blended films

Optimized blended 珡lms	μ_e ($cm^2 V^{-1} s^{-1}$)[a]	μ_h ($cm^2 V^{-1} s^{-1}$)[b]	μ_e/μ_h	$P(E,T)$ [c]	n[d]	S[e]
Ni-PDI:PBDB-TFCl	4.16×10^{-6}	2.36×10^{-7}	17.61	0.62	1.19	0.719
Pd-PDI:PBDB-TFCl	5.53×10^{-6}	3.29×10^{-8}	167.98	0.60	0.98	0.913
Pt-PDI:PBDB-TFCl	5.14×10^{-5}	1.44×10^{-6}	35.79	0.64	0.75	0.812
TTF-PDI:PBDB-TFCl	1.89×10^{-6}	3.56×10^{-8}	53.16	0.58	1.69	0.914
QU-PDI:PBDB-TFCl	4.41×10^{-4}	2.85×10^{-4}	1.55	0.98	1.45	0.995
PH-PDI:PBDB-TFCl	2.76×10^{-4}	4.46×10^{-5}	6.19	0.92	0.99	0.975

[a] Device structure of ITO/ZnO/PDI propellers:PBDB-TFCl/PDINO/Al for electrons. [b] Device structure of ITO/PEDOT:PSS/PDI propellers:PBDB-TFCl/MoO_3/Al for holes. [c] Exciton dissociation probability: $P(E,T) = J_{ph}/J_{sat}$. [d] The slope of V_{OC} 珐 $\ln(P_{light})$ is close to nkT/q. [e] The slope of J_{SC} 珐 P_{light}^{S}.

and 5.14×10^{-5} $cm^2 V^{-1} s^{-1}$ for Ni-PDI, Pd-PDI and Pt-PDI, respectively. The hole mobilities are 2.36×10^{-7} $cm^2 V^{-1} s^{-1}$, 3.29×10^{-8} $cm^2 V^{-1} s^{-1}$ and 1.44×10^{-6} $cm^2 V^{-1} s^{-1}$ for Ni-PDI, Pd-PDI and Pt-PDI, respectively. The hole mobilities of the three d^8 metal core PDI propeller blended 珡lms are much lower than their electron mobilities. For TTF-PDI, which does not have a metal core and possesses a molecular con珡guration similar to that of Ni-PDI, Pd-PDI and Pt-PDI, both the electron and hole mobilities of the blended 珡lms remain at relatively low values of 1.89×10^{-6} $cm^2 V^{-1} s^{-1}$ and 3.56×10^{-8} $cm^2 V^{-1} s^{-1}$, respectively. It can be seen that the unbalanced carrier transport properties (μ_e/μ_h) of Ni-PDI (17.61), Pd-PDI (167.98), Pt-PDI (35.79) and TTF-PDI (53.16) may partially explain their low FF values. For the PBDB-TFCl:PH-PDI blended 珡lm, the electron and hole mobility are 2.76×10^{-4} $cm^2 V^{-1} s^{-1}$ and 4.46×10^{-5} $cm^2 V^{-1} s^{-1}$ with μ_e/μ_h ¼ 6.19. For the PBDB-TFCl:QU-PDI blended 珡lm, the electron and hole mobilities increase to 4.41×10^{-4} $cm^2 V^{-1} s^{-1}$ and 2.85×10^{-4} $cm^2 V^{-1} s^{-1}$ with μ_e/μ_h ¼ 1.55. The increased electron and hole mobilities with balanced carrier transport properties from the d^8 metal and TTF cores to the phenyl and benzoquinone core PDI propeller blended 珡lms (with the PBDB-TFCl donor polymer) are bene珡cial to charge transport and improving the photovoltaic performance. The electron and hole carrier mobilities of the six PDI propeller blended 珡lms are connected to the intramolecular charge trap effect, which will be discussed later.

To further clarify the differences in the J_{SC} and FF of the six OPV devices, the photogenerated current density (J_{ph}) *versus* the effective voltage (V_{eff}) was investigated, which is plotted in Fig. S47† and summarized in Table 3.[56] Under the short-circuit condition, the d^8 metal and TTF core PDI propeller-based devices exhibit an extremely low exciton dissociation probability $P(E,T) = J_{ph}/J_{sat}$ of 0.58 to 0.64. This suggests that photogenerated excitons in the devices based on the d^8 metal and TTF cores are inefficient to dissociate into free electrons and holes, which lead to their low J_{SC}. The $P(E,T)$ values for the blend 珡lm of PBDB-TFCl:QU-PDI and PBDB-TFCl:PH-PDI are 0.98 and 0.92, which are higher than those of d^8 metal core PDI propellers and TTF-PDI. This indicates that highly efficient exciton dissociation occurs at interfaces between PDI propellers and PBDB-TFCl, which is also consistent with the improved J_{SC} and FF of the QU-PDI and PH-PDI-based OPV devices.

The charge recombination that occurs in the devices was also investigated by measuring J_{SC} and V_{OC} with different light intensities (P_{light}) (Fig. S28†). As shown in Table 3, the relationship between V_{OC} and P_{light} can be described as V_{OC} 珐 $\ln(P_{light})$.[57,58] When monomolecular recombination dominates, the slope is close to $2kT/q$, where q, T and k are the elementary charge, Kelvin temperature and Boltzmann constant, respectively.[59] When bimolecular recombination dominates, the slope is close to $1kT/q$.[60] When surface recombination dominates, the slope is close to $0.5kT/q$.[57] The slope of Ni-PDI, Pd-PDI and Pt-PDI are $1.19kT/q$, $0.98kT/q$ and $0.75kT/q$, respectively. Clearly, the slope gradually decreases with heavier metal cores from Ni, Pd to Pt, suggesting that the recombination process dominating in the devices changes from bimolecular recombination to surface recombination. The slopes obtained for the TTF-PDI and QU-PDI blends are $1.69kT/q$ and $1.45kT/q$, respectively, suggesting that bimolecular and monomolecular recombination processes exist in the devices with less surface recombination. For PH-PDI, bimolecular recombination dominates in the devices with a slope of $0.99kT/q$. The J_{SC} value follows a power-law dependence with respect to P_{light}, which can be described as J_{SC} 珐 P_{light}^{S}.[61,62] Herein, S ¼ 1 indicates that all free carriers are collected and swept out at the electrodes prior to recombination. However, $S < 1$ indicates some extent of bimolecular recombination.[59,60] The values of S for Ni-PDI, Pd-PDI, Pt-PDI and TTF-PDI blends are 0.719, 0.913, 0.812 and 0.914, respectively, which indicates strong bimolecular recombination. The QU-PDI and PH-PDI propellers with S values of 0.995 and 0.975 exhibit less bimolecular recombination than the other four PDI propellers, which is consistent with their excellent OPV performances. These dissociation and recombination efficiencies of the six PDI propeller-based devices with similar con珡gurations vary with six distinct cores, which ultimately leads to tremendous differences in the OPV performance.

2.6 Intramolecular charge trap

The OPV performances based on the QU-PDI and PH-PDI acceptors are up to more than 300 times higher than those of the d^8 metal core PDI propeller acceptors. The subtle difference in the six four-bladed PDI propellers is that they have varied core structures. To determine how the central core subunits interact to generate electronic behaviours and affect the OPV properties, the Frontier orbital levels of the blade PDI and core subunits were investigated using DFT calculations (Computational details in Fig. S51†).

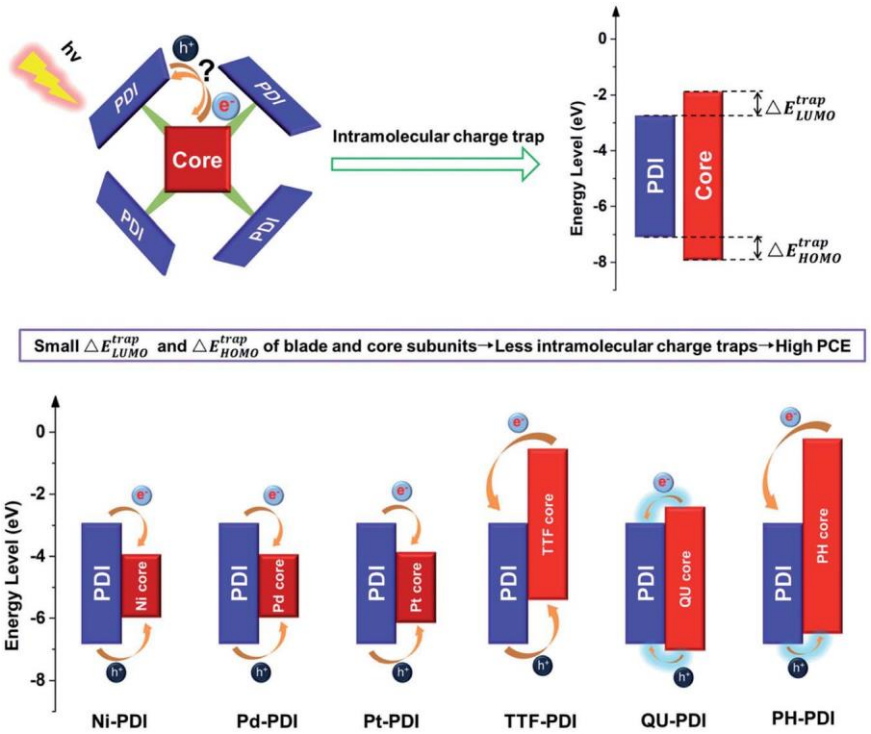

Fig. 6 Schematic diagram of an intramolecular charge trap in the six four-bladed PDI propellers with d^8 metal and non-metal cores.

An intermolecular charge trap between the donor/acceptor and the third component could seriously reduce the PCEs. For ternary OPVs with one acceptor/two donors or one donor/two acceptors, the third component should have similar HOMO or LUMO levels compared with those of the host donor and acceptor. The similar HOMO or LUMO levels of the two donors or acceptors can prohibit deep charge trap from forming to achieve better charge transport and a high PCE.[63,64] Generally, in a molecule, all the atomic orbitals are mainly hybridized into molecular orbitals, and thus, the charge transfer that occurs within a molecule is the excitation of an electron from the HOMO to the LUMO. For complex molecular systems, such as dendrimers,[65] pentamer arrays,[66] subphthalocyanines and pentacene dimers,[67] *etc.*, all the atomic orbitals of the subunits are difficult to fully hybridize into molecular orbitals. Under such circumstances, the energy transfer behaviour between the varied subunits in photovoltaic materials greatly influences the exciton generation/dissociation/recombination process in the donor–acceptor heterojunction structures and their OPV performance, which is rarely studied. Herein, we deduce that the charge trap effect in ternary OPVs also exist in binary OPVs. The schematic diagram of the intramolecular charge trap about six four-bladed PDI propellers with d^8 metal and non-metal cores is depicted in Fig. 6. The Frontier orbital level data of

Table 4 Frontier orbital level data of the blade PDI and cores of the PDI propellers

Compounds[a]	LUMO (eV)	HOMO (eV)	DE^{trap}_{LUMO}[b] (eV)	DE^{trap}_{HOMO} (eV)	PCE (%)
Blade PDI	—3.10	—6.49	—	—	—
Core of Ni-PDI	—4.04	—5.77	0.94	0.72	0.07
Core of Pd-PDI	—4.08	—5.76	0.98	0.73	0.03
Core of Pt-PDI	—4.01	—5.92	0.91	0.58	0.06
Core of TTF-PDI	—0.81	—5.25	2.29	1.24	0.18
Core of QU-PDI	—2.63	—6.79	0.47	0.30	9.33
Core of PH-PDI	—0.49	—6.24	2.61	0.25	6.01
Core of BDT-PDI4[c]	—1.00	—6.12	2.10	0.37	6.1 (ref. 14)
Core of TPPz-PDI4[c]	—1.05	—6.19	2.05	0.30	7.1 (ref. 71)
Core of TTB-PDI4[c]	—1.09	—6.22	2.02	0.28	7.1 (ref. 14)

[a] Detailed structures and Frontier orbitals of the blade PDI and cores are shown in Fig. S52. The LUMO and HOMO levels are calculated by DFT. [b] DE^{trap}_{LUMO} and DE^{trap}_{HOMO} are determined by the formulas $DE^{trap}_{LUMO} = |E^{PDI}_{LUMO} - E^{core}_{LUMO}|$ and $DE^{trap}_{HOMO} = |E^{PDI}_{HOMO} - E^{core}_{HOMO}|$, where E^{PDI}_{LUMO} and E^{core}_{LUMO} are the LUMO levels of the blade PDI and cores of the PDI propellers, respectively, and E^{PDI}_{HOMO} and E^{core}_{HOMO} are the HOMO levels of the blade PDI and cores of the PDI propellers, respectively. [c] Four-bladed PDI propeller acceptors reported in the references. Detailed structures are shown in Fig. S52.

the blade PDI and cores of the PDI propellers are summarized in Table 4. The LUMO and HOMO levels of the PDI moiety are —3.10 eV and —6.49 eV, respectively. The cores of Ni-PDI, Pd-PDI and Pt-PDI have a narrower energy gap than the blade PDI. The values of $D E_{LUMO}^{trap}$ are as large as 0.91 eV to 0.98 eV. Additionally, for $D E_{HOMO}^{trap}$, the values are high, 0.72 eV, 0.73 eV and 0.58 eV for Ni-PDI, Pd-PDI and Pt-PDI, respectively. The cores of TTF-PDI, QU-PDI and PH-PDI have wider energy gaps than the blade PDI. TTF-PDI, which does not possess d^8 metal cores, exhibits a large $D E_{LUMO}^{trap}$ (2.29 eV) and $D E^{HOMO\ trap}$ (1.24 eV). Such high $D E_{LUMO}^{trap}$ and $D E_{HOMO}^{trap}$ values suggest that the devices based on the d^8 metal cores and TTF core suffer from a deep charge trap without efficient exciton dissociation, charge extraction, and collection processes, which is consistent with their low photovoltaic performance and poor photoresponse. For QU-PDI, the values of $D E_{LUMO}^{trap}$ and $D E_{HOMO}^{trap}$ are as low as 0.47 eV and 0.30 eV. Although the $D E_{LUMO}^{trap}$ of PH-PDI is as high as 2.61 eV, the value of $D E_{HOMO}^{trap}$ is only 0.25 eV, which is low. Such similar HOMO and LUMO levels between the blade PDI and core subunits endow the QU-PDI and PH-PDI with fewer charge traps, resulting in better charge transport and high PCEs for use as excellent solar cell acceptors.

Steady-state and transient photoluminescence (PL) measurements are performed to verify the intramolecular charge trap in the six four-bladed PDI propellers. As shown in Fig. 7A, strong PL emission from QU-PDI and PH-PDI can be observed with emission peaks around 660 nm. The other four PDI propellers exhibit weak PL emissions, indicating that a strong intramolecular charge trap exists between the PDI moiety and core subunits. Fig. 7B shows the time resolved transient PL spectra of the PDI propeller 珺lms. The emission lifetime of 660 nm in the Ni-PDI, Pd-PDI, Pt-PDI and TTF-PDI 珺lms is 0.64–1.67 ns, which is much lower than the emission lifetime of 3.87 ns and 3.30 ns in the QU-PDI and PH-PDI 珺lms, respectively, suggesting that exciton dissociation, charge transfer and intramolecular charge trap process occur at the PDI moiety and core subunits.[65,68] The steady-state and transient PL measurements performed on the blended 珺lms are also shown in Fig. S44.† The PL emission of PBDB-TFCl is effectively quenched by the six PDI propellers in the blended 珺lms. The emission lifetime of the blended 珺lms is 0.59–0.74 ns, which is lower than that of their neat PDI propeller 珺lms, suggesting that exciton dissociation and charge transfer also occur at the donor/acceptor interfaces.[69,70] Summarizing the results of the transient PL experiments, the intramolecular charge trap between the blade and core subunits makes the strong 琢uorescence PDI unit become a weak emitter and shortens the PL lifetime of the PDI propellers. This is unfavourable for excitons dissociating into free carriers in the bulk heterojunction structures.

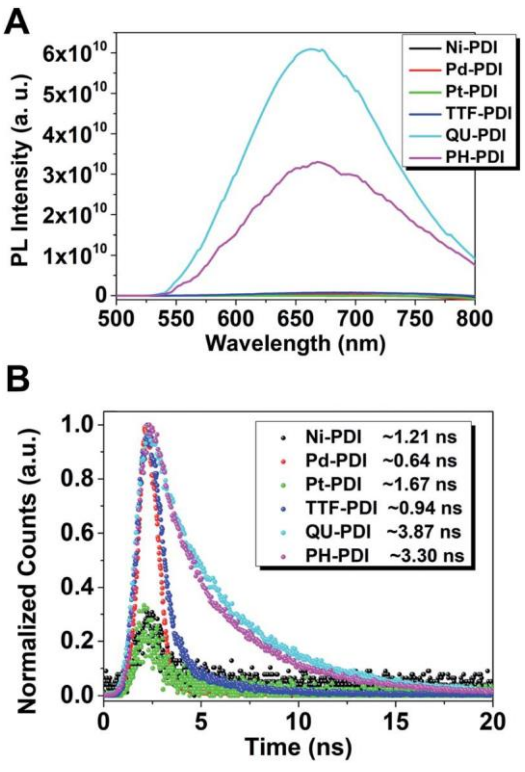

Fig. 7 (A) PL measurements obtained for the PDI propellers films and (B) transient PL of the PDI propellers films in response to 450 nm pulses (excited at 450 nm and monitored at 660 nm). The PL emission of Ni-PDI and Pt-PDI is too weak to obtain distinct transient PL data. Steady-state and transient PL measurements performed on the blended films, as shown in Fig. S44.†

The intramolecular charge trap can also be evidenced by the EQE spectra of the d^8 metal core and TTF core-based PDI propellers shown in Fig. 3E. The high EQE contributions in the donor and acceptor regions indicate efficient exciton dissociation, charge transport and collection from the devices.[17] The low EQE response around 530 nm (strong absorption band of the PDI moiety) and no EQE response in the NIR range (strong absorption band of the d^8 metal cores) for the d^8 metal PDI propeller-based devices is in connection with the trap effects between the PDI blade and d^8 metal cores. TTF-PDI with the organic TTF core also has a very low current density and low EQE values. An important reason is that the TTF core with a highly upshi沃ed energy level endows obvious trap effects in the TTF-PDI based devices. For ternary OPVs, a deep intermolecular charge trap between the third compound and the host donor/acceptor could decrease the electron and hole mobilities of the ternary active layer with unbalanced carrier transport properties.[72–75] Recently reported results by Yan even prove that small energetic offsets of the third donor compound could assist electron transport of the BHJ layer in ternary OPVs.[55] Herein, we have uncovered a similar phenomenon in binary OPVs: an intramolecular charge trap. As shown in Table 4, the trap effects between the blade PDI moiety and core subunit (d^8 metal structures) also result in a large decrease in the electron and hole mobilities of the d^8 metal PDI propeller-based BHJ layer and losses of the balanced carrier transport properties in binary OPVs. Eventually, Ni-PDI, Pd-PDI, Pt-PDI and TTF-PDI with deep intramolecular charge trap effects exhibit poor OPV performances. These intrinsic differences in the core subunits and corresponding orbital levels correlate well with such drastic variations observed in BHJ solar cells.

The $D E_{LUMO}^{trap}$ and $D E_{HOMO}^{trap}$ values of the high performance four-bladed PDI propeller acceptors BDT-PDI4, TPPz-PDI4 and

TTB-PDI4, as reported by Yan,[14,71] were also calculated for comparison. The detailed structures of these four-bladed PDI propeller acceptors are shown in Fig. S52,† and the relative data are summarized in Table 4. The values of $D E_{LUMO}^{trap}$ for BDT-PDI4, TPPz-PDI4 and TTB-PDI4 are 2.10 eV, 2.05 eV and 2.02 eV, respectively. The values of $D E_{HOMO}^{trap}$ for BDT-PDI4, TPPz-PDI4 and TTB-PDI4 are 0.37 eV, 0.30 eV and 0.28 eV, respectively. As $D E_{LUMO}^{trap}$ and $D E_{HOMO}^{trap}$ decrease, the PCEs of the BDT-PDI4, TPPz-PDI4 and TTB-PDI4 acceptor-based OPV devices, blended with donor polymer P3TEA, increase from 6.1% to 7.1%. In particular, ring-fused PDI propellers with enhanced rigidity have been reported as a promising strategy to improve the PCE.[3,14] One possible reason can be ascribed to the increased repulsive molecular interactions and lower miscibility between the polymer donor and PDI acceptor, leading to an improved average domain purity.[14] Herein, we deduce that ring-fused structures can also increase the intramolecular orbital overlap of the subunits in PDI propellers. With the ring-fused strategy, the intramolecular charge trap between the PDI blades and core subunits can be suppressed. This is another important reason for the enhanced PCEs of ring-fused PDI propeller acceptors (compared to non-fused PDIs). To the best of our knowledge, due to the fewer intramolecular charge traps of QU-PDI, the PCE of 9.33% is among the best results (PCE > 9%) for efficient OPV cells based on PDI acceptors (see Fig. S50 and Table S7†). These results demonstrate that low $D E_{LUMO}^{trap}$ and $D E_{HOMO}^{trap}$ PDI propellers with fewer intramolecular charge traps are a promising strategy for designing analogous PDI acceptors and would be a good reference when designing other types of donors or non-fullerene acceptors.

2.7 Electrocatalytic hydrogen evolution

Water electrolysis driven by renewable resource-derived electricity and direct solar-to-hydrogen conversion based on photochemical and photoelectrochemical water splitting is a promising pathway for sustainable hydrogen production. The development of artificial photosynthesis and electrochemical systems require highly active H_2 evolution catalysts with minimized overpotentials.[24,76–78] 0D, 1D and 2D metal dithiolene complexes are active photocatalytic and electrochemical HER catalysts.[21] As abovementioned, the OPV performances of the three PDI propellers with d^8 metal cores are quite poor, with PCE ≈ 0.03–0.07%. Considering that Ni-PDI, Pd-PDI, and Pt-PDI are functionalized with d^8 metal cores, there could be advantages in electrocatalytic fields that need to be developed for these PDI propellers. Moreover, the electrochemical HER of PDI dyes has never been investigated in previous reports. Next, we tried to use these materials to conduct electrocatalytic hydrogen evolution.

A three-electrode electrochemical cell was adopted to perform linear sweep voltammetry (LSV) in a 0.5 M H_2SO_4

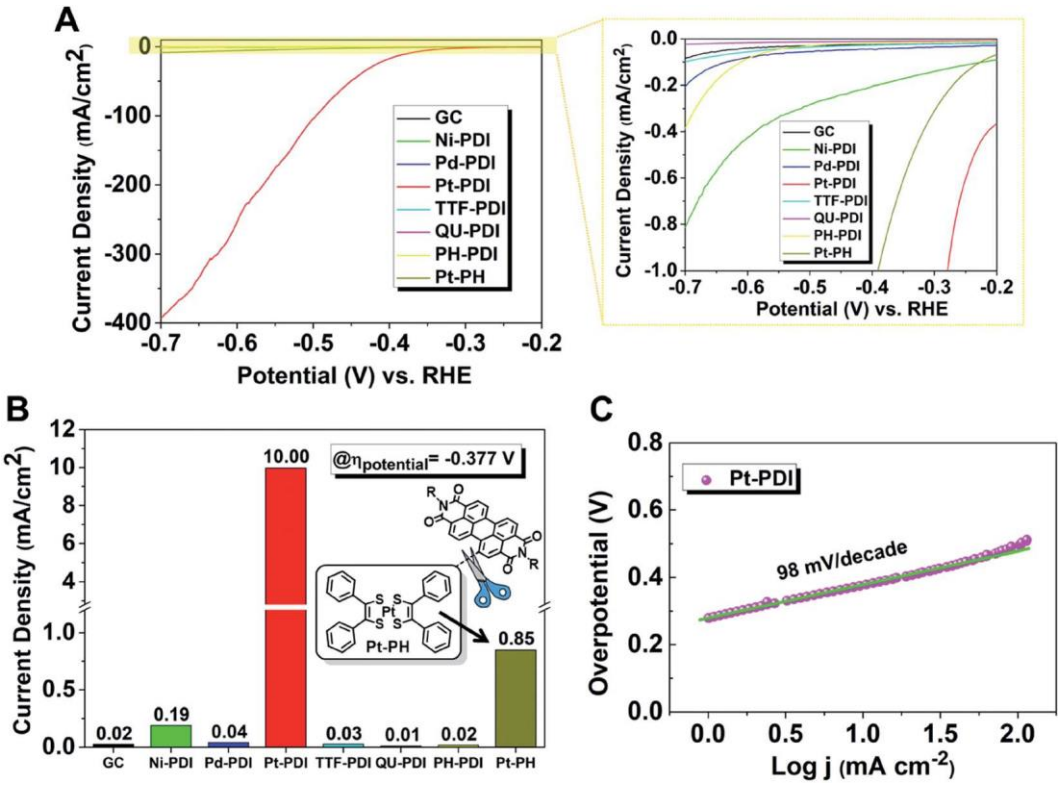

Fig. 8 HER performances of the six PDI propellers and Pt-PH without a PDI moiety. (A) The polarization curves for the six four-bladed PDI propellers, Pt-PH electrodes and glassy carbon electrode in the 0.5 M H_2SO_4 solution obtained with a scan rate of 10 mV s^{-1}. GC: glassy carbon electrode. (B) Comparisons of the HER reactivity at −0.377 V (*versus* RHE) for the six PDI propellers and Pt-PH catalysts. (C) Tafel plot of the Pt-PDI electrode.

solution to examine the electrochemical hydrogen production performance of the six four-bladed PDI propellers. Fig. 8A shows that Pt-PDI has an excellent electrocatalytic hydrogen production performance. The operating potential of Pt-PDI at 10 mA cm^{-2} was determined to be —0.377 V. Therefore, the speci珡c activity of each catalyst was calculated from the polarization curves at –0.377 V. As shown in Fig. 8B, the HER activities for the Ni-PDI and Pd-PDI catalysts are 0.19 mA cm^{-2} and 0.04 mA cm^{-2}, respectively, at the overpotential of —0.377 V. Furthermore, the HER activities of the non-metal core PDI propellers TTF-PDI, QU-PDI and PH-PDI are 0.03 mA cm^{-2}, 0.01 mA cm^{-2} and 0.02 mA cm^{-2}, respectively. Remarkably, the HER activity of the Pt-PDI catalyst is approximately up to 1000 times greater than that of the other 珡ve PDI propeller catalysts. These results suggest that the Pt 5d^8 metal dithiolene core can signi珡cantly increase the HER activity of the PDI propellers in comparison to the low HER activity rylene dyes. As shown in Fig. 8C, the Tafel slope value of Pt-PDI was 98.6 mV per decade, which means that the rate-determining step in the HER process was the Volmer reaction ($H_3O^+ + e^- \rightarrow H_{ads} + H_2O$).[79]

It has been proved that the coordination environments of metal atoms in complexes greatly affect their HER catalytic activity.[77,80,81] To understand the exceptional catalytic activity of PDI propellers, we investigated the Gibbs free energy pro珡les of three d^8 metal PDI catalysts by using the DFT calculations shown in Fig. 9A. The Gibbs free energy for the hydrogen adsorption (ΔG_{H^*}) of Pd-PDI and Ni-PDI is as large as 2.28 eV and 0.96 eV, respectively, indicating that H* is less efficiently able to adsorb on the metal complexes. However, Pt-PDI has the smallest ΔG_{H^*} value of 0.59 eV, indicating that efficient H* adsorption and recombination renders Pt-PDI an excellent electro-catalyst for HER. As shown in Fig. 9B, the HER activity of the d^8 metal in the PDI propellers increases according to the order of Pd 4d^8 < Ni 3d^8 « Pt 5d^8, as obtained from the results of the HER measurements and DFT analysis. This is because the total unoccupied density of states of the Pt 5d^8 orbital is closely related to the hydride formation, which can interact with the 1s orbital of the hydrogen atom and transfer electrons to the hydrogen atom.[80]

Additionally, the roles of the PDI moieties in Pt-PDI were also investigated by comparing to other Pt complexes that use benzene as ligands (denoted as Pt-PH, as shown in Fig. 8B). The HER activity of Pt-PDI is 10 times higher than that of Pt-PH, which indicates that the ligands also greatly affect the HER performance. Considering that the HER active sites of Pt-PDI and Pt-PH are both the same metal core with similar intrinsic activities, the main source of the difference in the catalytic performances is the number of catalytic active sites. The capacitance measurements were used to characterize the electrochemical surface areas of Pt-PDI and Pt-PH. The result in Fig. 9C shows that the slope obtained for Pt-PDI is obviously higher than the slope obtained for Pt-PH, which means that the electrochemical surface area of Pt-PDI is much larger than that of Pt-PH. The larger electrochemical surface areas indicate more exposed active sites, which is consistent with the HER activity.[82–84] As far as we know, four-bladed PDI propellers exhibit large steric hindrances, which is bene珡cial to reduce the aggregation of Pt-PDI. However, Pt-PH can easily form

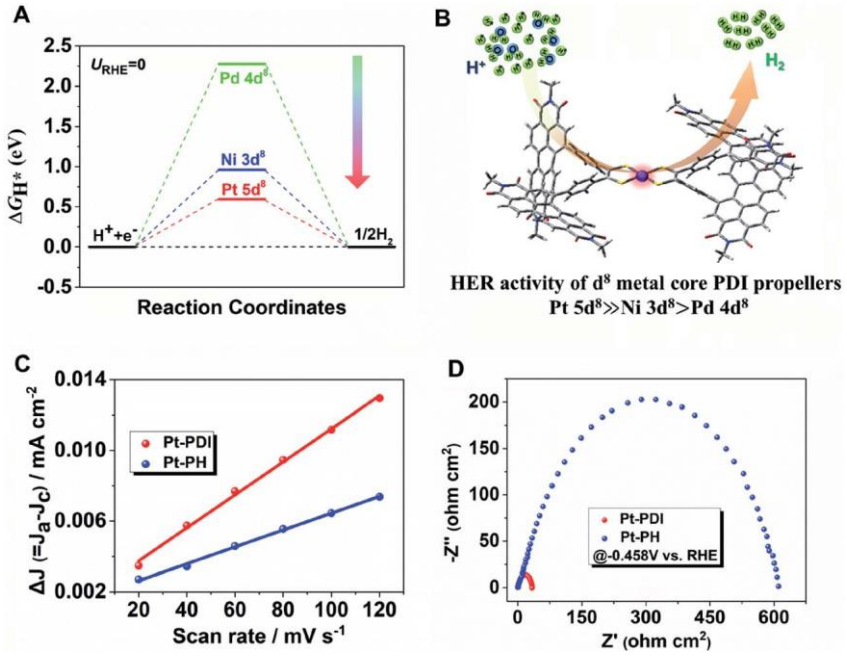

Fig. 9 Calculated Gibbs free-energy diagram and schematic illustration of the d^8 metal core PDI catalysts. (A) Calculated Gibbs free-energy diagram of the HER at an equilibrium potential. (B) Schematic illustration of the four-bladed PDI propellers with d^8 metal core catalysts for the HER. (C) DJ (¼J_a – J_c) of Pt-PDI and Pt-PH plotted against the scan rates, as shown in Fig. S38.† The slopes were used to represent the electrochemical surface areas of the HER. The unit of the slopes is F cm^{-2}. (D) Nyquist plots of the Pt-PDI and Pt-PH samples for the HER in 0.5 M H_2SO_4.

dimers,[85-87] leading to the aggregation of catalysts, which could decrease the number of active sites to result in a lower catalytic activity. Additionally, the electrochemical impedance spectroscopy analysis (Fig. 9D) indicates that the charge-transfer resistance of Pt-PDI is quite smaller than that of Pt-PH, confirming the faster charge-transfer process of Pt-PDI for hydrogen evolution. Therefore, from the abovementioned results, it can be concluded that Pt is the active centre of hydrogen production, and the PDI ligands reduce the aggregation of Pt complexes due to the large steric hindrance effect of the PDI moieties and propeller architectures. As a result, the 0D metal complex of Pt-PDI exhibits a record high electro-catalytic H_2 evolution activity among the reported rylene-based HER catalysts to date.

Conclusions

In conclusion, we have designed and synthesized three d^8 metal bis-dithiolene core-based and three non-metal core-based four-bladed PDI propellers. Ni-PDI, Pd-PDI and Pt-PDI with d^8 metal bis-dithiolene structures exhibit two absorption bands at 350–650 nm and 780–1200 nm with deep LUMO levels of —4.40 eV to —4.51 eV. The three non-metal core PDI propellers, TTF-PDI with a tetrathiafulvalene core, QU-PDI with a benzoquinone core, and PH-PDI with a benzene core, exhibit only one strong absorption band at 350–650 nm with higher LUMO levels of approximately —3.88 eV to —4.03 eV. For TTF-PDI, the intramolecular charge transfer complexes between the PDI blade and tetrathiafulvalene core can be evidenced by the NIR absorption band at approximately 914 nm. The OPV performances show that the QU-PDI and PH-PDI-based devices exhibit significantly enhanced V_{OC}, J_{SC} and FF values (compared to those devices based on a d^8 metal core and TTF core PDI propellers) due to the reduced intramolecular charge traps. This can be ascribed to the narrow Frontier orbital level gaps (both LUMO and HOMO) between the blade PDI and core subunits of the PDI propellers. The mobility data show that the QU-PDI and PH-PDI blends exhibit higher and balanced electron and hole mobilities, which are consistent with the small Frontier orbitals level gaps between the blade PDI and core subunits. As a result, the QU-PDI and PH-PDI acceptors exhibit up to more than 300 times higher PCEs (9.33%) than those of the d^8 metal core PDI propellers (Pd-PDI, PCE ¼ 0.03%), indicating that the QU-PDI and PH-PDI acceptors exhibit one of the best photovoltaic performances with an excellent fill factor (FF ¼ 71.8%) among PDI-derivative acceptors. These results demonstrate that PDI propellers with reduced Frontier orbital level gaps (both LUMO and HOMO) between the blade and core subunits are promising for use in electron acceptors in non-fullerene OPVs and would be a general strategy that can be exploited to design the next generation of PDI-based photovoltaic materials. Additionally, the HER activity of the PDI propellers with d^8 metal cores as metal complex catalysts increases according to the order of Pd $4d^8$ < Ni $3d^8$ « Pt $5d^8$. In contrast to the OPV performances, the HER activity of the Pt-PDI catalyst is up to approximately 1000 times greater than that of the other five PDI propeller catalysts. The effective d^8 metal core in the PDI propellers offers exciting prospects for the molecular design of rylene-based HER catalysts. These systematic studies on the core effect of PDI propellers will expand the scope of rylene architectures, facilitating their applications in OPVs, HERs and other related potential fields.

Conflicts of interest

There are no conflicts to declare.

Acknowledgements

The authors are deeply grateful to the Youth Innovation Promotion Association CAS (2016194) and the National Natural Science Foundation of China (51773220 and 51573205), the Shandong Provincial Natural Science Foundation (ZR2017ZB0314), DICP & QIBEBT (UN201709) and the Dalian National Laboratory for Clean Energy (DNL) CAS for their financial support. This work was partially supported by the State Key Laboratory of Fine Chemicals (KF1814). The authors also thank the beamline BL16B1 and Prof. Chunming Yang of Shanghai Synchrotron Radiation Facility for providing the beam time and useful discussion.

Notes and references

1 D. Meng, H. Fu, C. Xiao, X. Meng, T. Winands, W. Ma, W. Wei, B. Fan, L. Huo, N. L. Doltsinis, Y. Li, Y. Sun and Z. Wang, *J. Am. Chem. Soc.*, 2016, 138, 10184–10190.
2 D. Meng, G. Liu, C. Xiao, Y. Shi, L. Zhang, L. Jiang, K. K. Baldridge, Y. Li, J. S. Siegel and Z. Wang, *J. Am. Chem. Soc.*, 2019, 141, 5402–5408.
3 J. Zhang, Y. Li, J. Huang, H. Hu, G. Zhang, T. Ma, P. C. Y. Chow, H. Ade, D. Pan and H. Yan, *J. Am. Chem. Soc.*, 2017, 139, 16092–16095.
4 G. Liu, T. Koch, Y. Li, N. L. Doltsinis and Z. Wang, *Angew. Chem., Int. Ed.*, 2019, 58, 178–183.
5 C. Yan, S. Barlow, Z. Wang, H. Yan, A. K. Y. Jen, S. R. Marder and X. Zhan, *Nat. Rev. Mater.*, 2018, 3, 18003.
6 P. Cheng, G. Li, X. Zhan and Y. Yang, *Nat. Photonics*, 2018, 12, 131–142.
7 X. Fan, J. Gao, W. Wang, S. Xiao, C. Zhan, X. Lu and Q. Zhang, *Chem.–Asian J.*, 2019, 14, 1814–1822.
8 W. Chen and Q. Zhang, *J. Mater. Chem. C*, 2017, 5, 1275–1302.
9 X. Zhan, Z. a. Tan, B. Domercq, Z. An, X. Zhang, S. Barlow, Y. Li, D. Zhu, B. Kippelen and S. R. Marder, *J. Am. Chem. Soc.*, 2007, 129, 7246–7247.
10 Z. Liu, Y. Wu, Q. Zhang and X. Gao, *J. Mater. Chem. A*, 2016, 4, 17604–17622.
11 X. Zhan, A. Facchetti, S. Barlow, T. J. Marks, M. A. Ratner, M. R. Wasielewski and S. R. Marder, *Adv. Mater.*, 2011, 23, 268–284.
12 H. Sun, X. Song, J. Xie, P. Sun, P. Gu, C. Liu, F. Chen, Q. Zhang, Z. K. Chen and W. Huang, *ACS Appl. Mater. Interfaces*, 2017, 9, 29924–29931.
13 J. Wang and X. Zhan, *Trends in Chemistry*, 2019, 1, 869–881.

14 H. Hu, Y. Li, J. Zhang, Z. Peng, L.-k. Ma, J. Xin, J. Huang, T. Ma, K. Jiang, G. Zhang, W. Ma, H. Ade and H. Yan, *Adv. Energy Mater.*, 2018, 1800234, DOI: 10.1002/aenm.201800234.
15 N. Liang, K. Sun, Z. Zheng, H. Yao, G. Gao, X. Meng, Z. Wang, W. Ma and J. Hou, *Adv. Energy Mater.*, 2016, 6, 1600060.
16 Z. Luo, T. Liu, Z. Chen, Y. Xiao, G. Zhang, L. Huo, C. Zhong, X. Lu, H. Yan, Y. Sun and C. Yang, *Adv. Sci.*, 2019, 1802065, DOI: 10.1002/advs.201802065.
17 L. Yang, W. Gu, L. Lv, Y. Chen, Y. Yang, P. Ye, J. Wu, L. Hong, A. Peng and H. Huang, *Angew. Chem., Int. Ed.*, 2017, 1096–1102, DOI: 10.1002/anie.201712011.
18 A. Zhang, C. Li, F. Yang, J. Zhang, Z. Wang, Z. Wei and W. Li, *Angew. Chem., Int. Ed.*, 2017, 56, 2694–2698.
19 J. Liu, S. Chen, D. Qian, B. Gautam, G. Yang, J. Zhao, J. Bergqvist, F. Zhang, W. Ma, H. Ade, O. Inganäs, K. Gundogdu, F. Gao and H. Yan, *Nat. Energy*, 2016, 1, 16089.
20 B. Garreau-de Bonneval, K. I. Moineau-Chane Ching, F. Alary, T.-T. Bui and L. Valade, *Coord. Chem. Rev.*, 2010, 254, 1457–1467.
21 T. Kusamoto and H. Nishihara, *Coord. Chem. Rev.*, 2019, 380, 419–439.
22 R. Dong, M. Pfeffermann, H. Liang, Z. Zheng, X. Zhu, J. Zhang and X. Feng, *Angew. Chem., Int. Ed.*, 2015, 54, 12058–12063.
23 K. Koshiba, K. Yamauchi and K. Sakai, *Angew. Chem., Int. Ed.*, 2017, 56, 4247–4251.
24 C. A. Downes and S. C. Marinescu, *J. Am. Chem. Soc.*, 2015, 137, 13740–13743.
25 K. Wang and E. I. Stiefel, *Science*, 2001, 291, 106–109.
26 G. N. Schrauzer, *Recent Advances in the Chemistry of Transition Metal Complexes of Unsaturated Bidentate Sulfur Donor Ligands (Metal Dithienes)*, ACS Publications, 1972, pp. 73–78.
27 Y. F. Zeng, X. Hu, F. C. Liu and X. H. Bu, *Chem. Soc. Rev.*, 2009, 38, 469–480.
28 W. R. McNamara, Z. J. Han, C. J. Yin, W. W. Brennessel, P. L. Holland and R. Eisenberg, *Proc. Natl. Acad. Sci. U. S. A.*, 2012, 109, 15594–15599.
29 D. Khusnutdinova, B. L. Wadsworth, M. Flores, A. M. Beiler, E. A. R. Cruz, Y. Zenkov and G. F. Moore, *ACS Catal.*, 2018, 8, 9888–9898.
30 J. C. Wang, S. P. Hill, T. Dilbeck, O. O. Ogunsolu, T. Banerjee and K. Hanson, *Chem. Soc. Rev.*, 2018, 47, 104–148.
31 G. N. Schrauzer and V. P. Mayweg, *J. Am. Chem. Soc.*, 1965, 87, 1483–1489.
32 D. G. Branzea, F. Pop, P. Auban-Senzier, R. Clerac, P. Alemany, E. Canadell and N. Avarvari, *J. Am. Chem. Soc.*, 2016, 138, 6838–6851.
33 Y. Mitamura, H. Yorimitsu, K. Oshima and A. Osuka, *Chem. Sci.*, 2011, 2, 2017–2021.
34 Z. Hassan, I. Ullah, I. Ali, R. A. Khera, I. Knepper, A. Ali, T. Patonay, A. Villinger and P. Langer, *Tetrahedron*, 2013, 69, 460–469.
35 G. Gao, N. Liang, H. Geng, W. Jiang, H. Fu, J. Feng, J. Hou, X. Feng and Z. Wang, *J. Am. Chem. Soc.*, 2017, 139, 15914–15920.
36 R. Perochon, L. Piekara-Sady, W. Jurga, R. Clerac and M. Fourmigue, *Dalton Trans.*, 2009, 3052–3061.
37 K. Walzer, B. Maennig, M. Pfeiffer and K. Leo, *Chem. Rev.*, 2007, 107, 1233–1271.
38 A. Mityashin, Y. Olivier, T. Van Regemorter, C. Rolin, S. Verlaak, N. G. Martinelli, D. Beljonne, J. Cornil, J. Genoe and P. Heremans, *Adv. Mater.*, 2012, 24, 1535–1539.
39 J. E. Cochran, M. J. N. Junk, A. M. Glaudell, P. L. Miller, J. S. Cowart, M. F. Toney, C. J. Hawker, B. F. Chmelka and M. L. Chabinyc, *Macromolecules*, 2014, 47, 6836–6846.
40 J. Gao, E. T. Niles and J. K. Grey, *J. Phys. Chem. Lett.*, 2013, 4, 2953–2957.
41 Z. G. Zhang, B. Y. Qi, Z. W. Jin, D. Chi, Z. Qi, Y. F. Li and J. Z. Wang, *Energy Environ. Sci.*, 2014, 7, 1966–1973.
42 X. Wang, K. Dou, B. Shahid, Z. Liu, Y. Li, M. Sun, N. Zheng, X. Bao and R. Yang, *Chem. Mater.*, 2019, 31, 6163–6173.
43 M. Renz, K. Theilacker, C. Lambert and M. Kaupp, *J. Am. Chem. Soc.*, 2009, 131, 16292–16302.
44 Y. Duan, X. Xu, H. Yan, W. Wu, Z. Li and Q. Peng, *Adv. Mater.*, 2017, 29, 1605115.
45 Z. Luo, T. Liu, W. Cheng, K. Wu, D. Xie, L. Huo, Y. Sun and C. Yang, *J. Mater. Chem. C*, 2018, 6, 1136–1142.
46 P. Muller-Buschbaum, *Adv. Mater.*, 2014, 26, 7692–7709.
47 T. E. Kang, H.-H. Cho, H. j. Kim, W. Lee, H. Kang and B. J. Kim, *Macromolecules*, 2013, 46, 6806–6813.
48 J. W. Lee, H. Ahn and W. H. Jo, *Macromolecules*, 2015, 48, 7836–7842.
49 J. Li, Y. Wang, Z. Liang, N. Wang, J. Tong, C. Yang, X. Bao and Y. Xia, *ACS Appl. Mater. Interfaces*, 2019, 11, 7022–7029.
50 Q. Wu, D. Zhao, M. B. Goldey, A. S. Filatov, V. Sharapov, Y. J. Colon, Z. Cai, W. Chen, J. de Pablo, G. Galli and L. Yu, *ACS Appl. Mater. Interfaces*, 2018, 10, 10043–10052.
51 X. Li, H. Wang, H. Nakayama, Z. Wei, J. A. Schneider, K. Clark, W.-Y. Lai, W. Huang, J. G. Labram, J. R. de Alaniz, M. L. Chabinyc, F. Wudl and Y. Zheng, *ACS Appl. Energy Mater.*, 2019, 2, 3805–3814.
52 D. Xia, C. Li and W. Li, *Chem. Rec.*, 2019, 19, 962–972.
53 N. Liang, X. Zhu, Z. Zheng, D. Meng, G. Liu, J. Zhang, S. Li, Y. Li, J. Hou, B. Hu and Z. Wang, *Chem. Mater.*, 2019, 31, 3636–3643.
54 Q. Wu, D. Zhao, A. M. Schneider, W. Chen and L. Yu, *J. Am. Chem. Soc.*, 2016, 138, 7248–7251.
55 H. Yin, L. K. Ma, Y. Wang, J. Huang, H. Yu, J. Zhang, P. C. Y. Chow, W. Ma, S. K. So and H. Yan, *Adv. Mater.*, 2019, 1903998, DOI: 10.1002/adma.201903998.
56 N. B. Kolhe, D. K. Tran, H. Lee, D. Kuzuhara, N. Yoshimoto, T. Koganezawa and S. A. Jenekhe, *ACS Energy Lett.*, 2019, 4, 1162–1170.
57 S. Solak, P. W. M. Blom and G. A. H. Wetzelaer, *Appl. Phys. Lett.*, 2016, 109, 053302.
58 X. Bao, Y. Zhang, J. Wang, D. Zhu, C. Yang, Y. Li, C. Yang, J. Xu and R. Yang, *Chem. Mater.*, 2017, 29, 6766–6771.
59 J. Wang, J. Zhang, Y. Xiao, T. Xiao, R. Zhu, C. Yan, Y. Fu, G. Lu, X. Lu, S. R. Marder and X. Zhan, *J. Am. Chem. Soc.*, 2018, 140, 9140–9147.
60 X. Zhang, C. Zhan and J. Yao, *Chem. Mater.*, 2014, 27, 166–173.

61 M. P. Hughes, K. D. Rosenthal, R. R. Dasari, B. R. Luginbuhl, B. Yurash, S. R. Marder and T. Q. Nguyen, *Adv. Funct. Mater.*, 2019, 1901269, DOI: 10.1002/adfm.201901269.
62 I. Riedel, J. Parisi, V. Dyakonov, L. Lutsen, D. Vanderzande and J. C. Hummelen, *Adv. Funct. Mater.*, 2004, 14, 38–44.
63 M. Zhang, Z. Xiao, W. Gao, Q. S. Liu, K. B. Jin, W. B. Wang, Y. Mi, Q. S. An, X. L. Ma, X. F. Liu, C. L. Yang, L. M. Ding and F. J. Zhang, *Adv. Energy Mater.*, 2018, 8, 1801968.
64 J. Lee, V. Tamilavan, K. H. Rho, S. Keum, K. H. Park, D. Han, Y. K. Jung, C. Yang, Y. Jin, J.-W. Jang, J. H. Jeong and S. H. Park, *Adv. Energy Mater.*, 2018, 8, 1702251.
65 T. T. Nguyen, D. Turp, D. Wang, B. Nolscher, F. Laquai and K. Mullen, *J. Am. Chem. Soc.*, 2011, 133, 11194–11204.
66 V. B. Yasarapudi, L. Frazer, J. E. A. Webb, J. K. Gallaher, A. Macmillan, A. Falber, P. Thordarson and T. W. Schmidt, *J. Phys. Chem. C*, 2018, 122, 13937–13943.
67 G. Lavarda, J. Zirzlmeier, M. Gruber, P. R. Rami, R. R. Tykwinski, T. Torres and D. M. Guldi, *Angew. Chem., Int. Ed.*, 2018, 57, 16291–16295.
68 X. Liu, Y. Yan, A. Honarfar, Y. Yao, K. Zheng and Z. Liang, *Adv. Sci.*, 2019, 6, 1802103.
69 Q. An, F. Zhang, W. Gao, Q. Sun, M. Zhang, C. Yang and J. Zhang, *Nano Energy*, 2018, 45, 177–183.
70 Y. Xie, F. Yang, Y. Li, M. A. Uddin, P. Bi, B. Fan, Y. Cai, X. Hao, H. Y. Woo, W. Li, F. Liu and Y. Sun, *Adv. Mater.*, 2018, 30, e1803045.
71 H. Lin, S. Chen, H. Hu, L. Zhang, T. Ma, J. Y. Lai, Z. Li, A. Qin, X. Huang, B. Tang and H. Yan, *Adv. Mater.*, 2016, 28, 8546–8551.
72 N. Gasparini, X. Jiao, T. Heumueller, D. Baran, G. J. Matt, S. Fladischer, E. Spiecker, H. Ade, C. J. Brabec and T. Ameri, *Nat. Energy*, 2016, 1, 16118.
73 L. Lu, W. Chen, T. Xu and L. Yu, *Nat. Commun.*, 2015, 6, 7327.
74 X. Ma, W. Gao, J. Yu, Q. An, M. Zhang, Z. Hu, J. Wang, W. Tang, C. Yang and F. Zhang, *Energy Environ. Sci.*, 2018, 11, 2134–2141.
75 F. Zhao, Y. Li, Z. Wang, Y. Yang, Z. Wang, G. He, J. Zhang, L. Jiang, T. Wang, Z. Wei, W. Ma, B. Li, A. Xia, Y. Li and C. Wang, *Adv. Energy Mater.*, 2017, 7, 1602552.
76 Q. Zuo, T. Liu, C. Chen, Y. Ji, X. Gong, Y. Mai and Y. Zhou, *Angew. Chem., Int. Ed.*, 2019, 131, 10304–10309.
77 X. P. Yin, H. J. Wang, S. F. Tang, X. L. Lu, M. Shu, R. Si and T. B. Lu, *Angew. Chem., Int. Ed.*, 2018, 57, 9382–9386.
78 F. Niu, D. Wang, F. Li, Y. Liu, S. Shen and T. J. Meyer, *Adv. Energy Mater.*, 2019, 1900399, DOI: 10.1002/aenm.201900399.
79 C. Chen, K. Yang, C. Liu, Y. Lu, C. Dong, D. Wei, S. Hu and R. Liu, *Nano Energy*, 2017, 32, 422–432.
80 N. Cheng, S. Stambula, D. Wang, M. N. Banis, J. Liu, A. Riese, B. Xiao, R. Li, T. K. Sham, L. M. Liu, G. A. Botton and X. Sun, *Nat. Commun.*, 2016, 7, 13638.
81 W. Lai, L. Zhang, W. Hua, S. Indris, Z. Yan, Z. Hu, B. Zhang, Y. Liu, L. Wang, M. Liu, Y. Wang, J. Wang, Z. Hu, H. Liu, S. Chou and S. Dou, *Angew. Chem., Int. Ed.*, 2019, 58, 11868–11873.
82 Z. Chen, X. Duan, W. Wei, S. Wang and B.-J. Ni, *J. Mater. Chem. A*, 2019, 7, 14971–15005.
83 X. Wang, W. Ma, C. Ding, Z. Xu, H. Wang, X. Zong and C. Li, *ACS Catal.*, 2018, 8, 9926–9935.
84 C. Hu, L. Zhang and J. Gong, *Energy Environ. Sci.*, 2019, 12, 2620–2645.
85 J. S. Pap, F. L. Benedito, E. Bothe, E. Bill, S. D. George, T. Weyhermuller and K. Wieghardt, *Inorg. Chem.*, 2007, 46, 4187–4196.
86 K. W. Browall, I. Lv and J. S. Kasper, *J. Am. Chem. Soc.*, 1971, 93, 6289.
87 C. E. Keefer, S. T. Purrington, R. D. Bereman and P. D. Boyle, *Inorg. Chem.*, 1999, 38, 5437–5442.

